Archive of Applied Mechanics 70 (2000) 255–268

Applicability of the Hertz contact theory to rail-wheel contact problems

W. Yan, F. D. Fischer

Summary Rail-wheel contact problems have been analyzed by applying three-dimensional finite element models. Based on these models, the applicability of the Hertz contact theory (HCT) to rail-wheel contact problems is verified in the present paper. Beside a standard rail, also a crane rail and a switching component are considered in the verification. In the case of a contact between the standard rail UIC60 and the standard wheel UICORE, different transverse contact positions are analyzed. Numerically calculated distributions of the contact pressure for different types of rails with respect to different initial contact positions agree with the results from the HCT only if either the contact zone does not spread into a region of changed surface curvature or if plastification does not occur. Finally, the convective part of the dissipation power due to friction is calculated, which cannot be provided directly by the HCT.

Key words Hertz contact theory, rail-wheel contact, elastic-plastic material

1
Introduction

Since Heinrich Hertz published his contact theory in 1882, [1], it has been extensively applied in many engineering fields which deal with contact problems. The application of the Hertz contact theory (HCT) in rail-wheel contact problems can be found also in the recent literature. For example, the HCT is applied in [2, 3] to investigate the growth of shell-type defects in the head of a railroad rail. Hertzian contact pressure is applied in a fatigue life model to describe the damage of wheels in [4]. An approximation of the HCT is used in the three-dimensional (3D) rail-fatigue model PHOENIX to describe the fatigue initiation in rail subsurface, [5], etc. The program CONTACT of the Delft group, [6, 7] can be considered as one of the most prominent programs in Europe for calculating the contact area and the corresponding deformation and stress state. However, CONTACT is based on the theory of an elastic halfspace.

Besides the HCT, a point load iteration method has recently been used to obtain the contact pressure in order to investigate the state of residual stress in a rail head, [8]. With the development of computational tools, numerical calculations have recently been extended to every corner of scientific research. For instance, a self-developed finite element (FE) code is applied in [9] to analyze rail-rolling contact fatigue cracks.

The HCT leads to an elliptical contact area and a semi-ellipsoid contact pressure distribution in the contact region. Due to its efficiency and simplicity, this theory has been extensively applied since its publication. However, as mentioned in [10], there are two limiting conditions for the applications of the HCT:

- the contact between elastic bodies should be frictionless,
- the significant dimensions of the contact area should be much smaller than the dimensions and the radii of curvature of the bodies in contact.

Received 5 August 1998; accepted for publication 6 May 1999

W. Yan
Christian-Doppler-Laboratorium für Funktionsorientiertes
Werkstoff-Design, Montanuniversität Leoben
A-8700 Leoben, Austria

F. D. Fischer
Institute of Mechanics, Montanuniversität Leoben
A-8700 Leoben, Austria

Correspondence to: F. D. Fischer

The first condition is approximately satisfied for rolling contact. Usually, the friction between the rail and the wheel can be considered separately, because its influence on the stress state introduced by the normal compressive load can be neglected.

The second condition is often violated, e.g. in the case of a switching component or for some special contact positions, such as gauge corner contact due to the transverse movement of the wheel axle. In this case, the contact zone may spread into regions of changed surface curvature. Moreover, plastic deformation can happen both in the wheel and in the rail, especially in cases with high axle loads.

In the last few years, a large number of 3D FE investigations were performed by our group applying ABAQUS, [11], for real rail/wheel/sleeper/bedding configurations. Based on this extensive study, the numerical results from the 3D FE calculations were compared to the HCT. Some interesting results concerning the application of the HCT to rail-wheel contact problems have been obtained, and will be presented in this paper.

2
Hertz contact theory

If two elastic nonconforming bodies contact together then, according to the HCT, [10], the contact area is elliptical in shape with a major semi-axis a and a minor semi-axis b. The distribution of the contact pressure in this elliptical area represents a semi-ellipsoid, which can be expressed as

$$p = p_0\left(1 - \frac{x^2}{a^2} - \frac{y^2}{b^2}\right), \qquad |x| \le a,\ |y| \le b\ . \tag{1}$$

Here, the origin of the coordinate system is located at the contact center, which is the initial contact point; p_0 is the largest contact pressure, which appears at the contact center; the x-axis extends along the major axis, and the y-axis along the minor axis. The values of p_0, a and b depend both on the external normal compressive force F perpendicular to the initial tangent plane and on the geometry of the contacting bodies near the contact region. Hertz assumed that the profiles of the contacting bodies near the contact region can be described by quadratic surfaces. Thus, the geometrical conditions are completely defined by the principal radii of curvature and their relative orientation at the initial contact point. Finally, p_0, a and b are determined by applying the following combinations of the principal radii of curvature:

$$\gamma_3 = \left[\left(\frac{1}{R_1'} + \frac{1}{R_2'}\right)\left(\frac{1}{R_1''} + \frac{1}{R_2''}\right) + \left(\frac{1}{R_1'} - \frac{1}{R_1''}\right)\left(\frac{1}{R_2'} - \frac{1}{R_2''}\right)\sin^2\varphi\right]^{1/2}\ , \tag{2}$$

$$\gamma_4 = \frac{1}{2}\left[\left(\frac{1}{R_1'} - \frac{1}{R_1''}\right)^2 + \left(\frac{1}{R_2'} - \frac{1}{R_2''}\right)^2 + 2\left(\frac{1}{R_1'} - \frac{1}{R_1''}\right)\left(\frac{1}{R_2'} - \frac{1}{R_2''}\right)\cos 2\varphi\right]^{1/2}\ , \tag{3}$$

$$\gamma_5 = \frac{1}{2}\left(\frac{1}{R_1'} + \frac{1}{R_1''}\right) + \frac{1}{2}\left(\frac{1}{R_2'} + \frac{1}{R_2''}\right)\ . \tag{4}$$

Here, R_1' and R_1'' are the minimum and maximum values, respectively, of the radius of curvature of the first body at the initial contact point, and R_2' and R_2'' are the corresponding values for body 2; the curvature radius is taken to be positive if the center of curvature lies within the body. Parameter φ is the angle between the principal normal sections with the minimum curvature radius in the first body and the second body. Tabular data from numerical computations for the values of p_0, a and b computed from γ_3, γ_4 and γ_5 can be found in [12]. The orientation angle α of the major axis of the contact ellipse relative to the principal normal section with minimum curvature radius of the first body can be determined by

$$\cos 2\alpha = -\frac{\left(\frac{1}{R_1'} - \frac{1}{R_1''}\right) + \left(\frac{1}{R_2'} - \frac{1}{R_2''}\right)\cos 2\varphi}{2\gamma_4}\ . \tag{5}$$

The maximum contact pressure p_0 and external normal compressive force F are related by a 1/3-power law, $p_0 \propto F^{1/3}$.

3
Verification

In our verification, three kinds of rails and their corresponding wheels are considered. The first one is a crane rail Cr135. The geometrical conditions for the application of the HCT are well satisfied in this case. Thus, this configuration is also a good example to check our numerical calculations.

The second one is the central component of a railway switch, named "frog". The wheel moves from a wing rail to a frog during a switching-over process. This switching is accompanied by a sudden change in the inclination of the wheel-center path and, therefore, by the transfer of a momentum to the frog. The minor principal curvature radius at the contact point of the frog is relatively small. We will check whether the HCT can be applied in this case.

Finally, a standard rail UIC60 is considered. The curvature radii of the cross-sectional profile are 300 mm, 80 mm and 13 mm. The initial contact position varies in practice due to the transverse shift of the wheel axle. Four typical transverse contact positions are considered both by the HCT and by 3D FE calculations.

Furthermore, results are presented for elastic-plastic material behavior which, of course, leads to a significant deviation from the HCT.

3.1
Crane rail Cr135

In this case, the initial contact point appears at the top point of the rail as the cross-sectional profile of the wheel is flat. Geometrical conditions are as follows: wheel $R_1' = 266.7$ mm, $R_1'' = \infty$; rail $R_2' = 355.0$ mm, $R_2'' = \infty$; $\varphi = 90^\circ$.

The rail and the wheel are assumed to be linear elastic with the same material data: $E = 210$ GPa and $\nu = 0.3$. The external normal compressive force F is 3.234×10^5 N. From Eqs. (3) and (5), we get $\cos 2\alpha = -1$ and $\alpha = 90^\circ$. That means the major axis of the contact ellipse lies in the transverse direction of the rail. After calculating the parameters γ_3, γ_4 and γ_5 from Eqs. (2), (3) and (4), the maximum contact pressure p_0, the major semi-axis a and the minor semi-axis b can be obtained from [12] as $p_0 = 2.1$ GPa, $a = 9.5$ mm, $b = 8.0$ mm. Inserting these values into Eq. (1), yields the distributions of the contact pressure along the major and minor semi-axes shown in Fig. 1 by dotted lines.

In our 3D FE calculation, only a quarter of the real configuration is modeled, according to the symmetry conditions. Figure 2 shows the FE mesh and the profile of the whole analyzed model for the rail CR135. The rail itself is bedded on rigid ground. Without affecting the contact configuration between the rail and the wheel, only a section of the wheel is simulated. Many truss elements with very high stiffness are used to connect the wheel axis and the upper surface of the wheel rim. A very fine mesh is constructed near the contact zone. Twenty-node quadratic brick elements are used for the wheel and the rail. Infinite elements are applied to reflect the constraint of the rail far away from the contact zone. The interface element INTER9

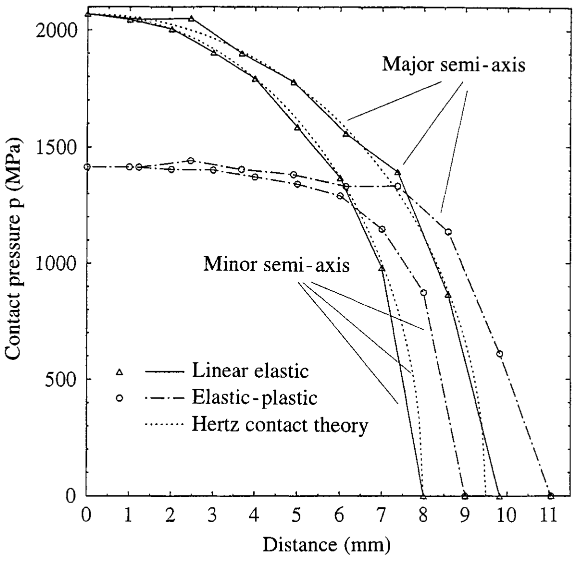

Fig. 1. Contact pressure distribution along the major and minor semi-axes of the Hertz contact ellipse for the crane rail Cr135 (major axis – rail's transverse direction; minor axis – rail's longitudinal direction)

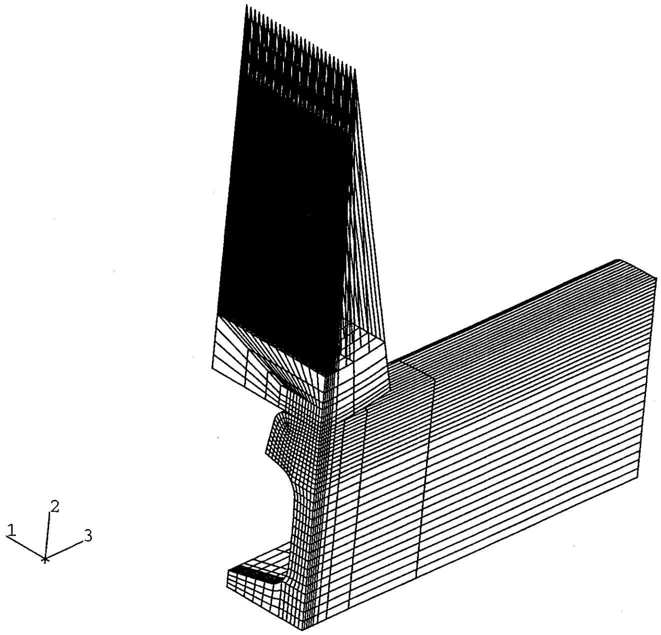

Fig. 2. Finite element mesh and the profile of the whole analyzed model for the crane rail CR135

is used to deal with the contact between the wheel and the rail, s. [11]. The whole model consists of 4609 elements with 60561 degrees of freedom. A complete calculation takes about 12 CPU hours on a modern high-speed processor. The numerical calculation indicates that the shape of the contact area looks very similar to an ellipse with the highest contact pressure in the central part. In order to compare quantitatively the distribution of contact pressure with the HCT, the numerical results of the contact pressure along the major semi-axis and the minor semi-axis of the Hertz contact ellipse are also shown in Fig. 1 with solid lines. The diagram shows that the numerical curve matches the theoretical curve from the HCT. Similar conclusions can be obtained from any path in the contact area. This means that the distribution of the contact pressure from the numerical calculation for elastic contact yields a semi-ellipsoidal distribution as described by Eq. (1). The special values of p_0, a and b extracted from the numerical calculation agree with those from the HCT. The major semi-axis a and the minor semi-axis b are much smaller than the geometrical parameters R'_1 and R'_2. The geometrical conditions of the Hertz contact theory are thus well satisfied in this example. This comparison indicates that our numerical calculation delivers satisfactory accuracy.

Using the same FE model, a numerical calculation of the elastic-plastic contact is carried out, too. In this calculation, only the material of the rail is assumed as elastic-plastic material described by a nonlinear kinematic hardening model, [13], with yield stresses $\sigma_{0.2} = 608$ MPa and $\sigma_{0.5} = 693$ MPa, etc. Although the shape of the contact area is still similar to an ellipse, the distribution of the contact pressure in the contact area is no longer semi-ellipsoidal. The variation of the contact pressure from the elastic-plastic calculation along the semi-axes of the theoretical ellipse is shown with dash-dotted lines in Fig. 1. The difference between the contact pressure distribution for elastic-plastic contact and the HCT results is obvious. The maximum contact pressure from the elastic-plastic contact analysis is much smaller than that from the HCT while the area of the contact zone has grown a little. As we can imagine, the pressure distribution is quite constant at the central part of the contact zone. The total contact force is obtained from the contact pressure in the whole contact area; although the area beneath the elastic-plastic curve in Fig. 1 is smaller than that beneath the linear-elastic curve, the normal compressive force F is the same in both calculations, due to the change of the contact area.

Figure 3 depicts the relation between the maximum pressure p_0 and the resultant normal compressive force F. It shows that a proportional relation, $p_0 \propto F^{1/3}$, exists for the numerical data of elastic contact when the normal compressive force is above 6000 N. A deviation in relation to the theoretical curve appears for small normal compressive forces. This shift may be caused by a rapid and discontinuous increase of the contact area at the initial loading state in the finite element calculation. It should be reduced by refining the mesh at the contact center. As the practical normal compressive force F exceeds the value in this stage, the range of deviation from the "Hertz line" is of no practical relevance due to the low level of F. Thus, it is not necessary to refine the mesh of our model. Comparing the elastic-plastic contact curve and

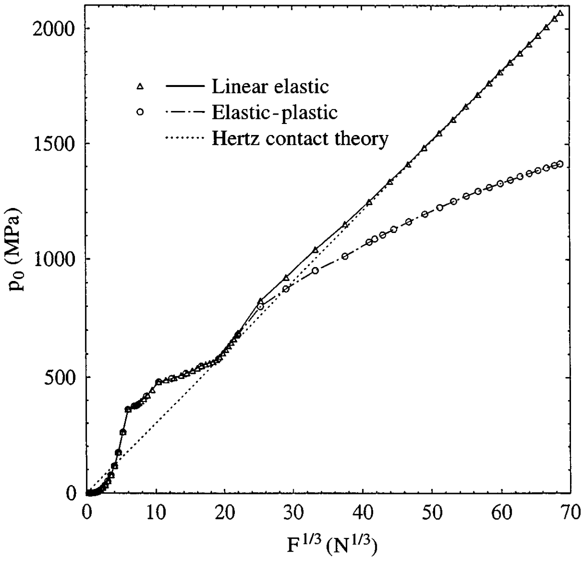

Fig. 3. Relation between the maximum contact pressure p_0 and the "1/3-power law" due to the external normal compressive force F for the crane rail Cr135

the elastic curve shows that the maximum contact pressure from the elastic-plastic calculation is always less than p_0 according to Hertz contact theory. This discrepancy becomes larger with an increasing external normal compressive force, i.e. with increasing plastic deformation in the rail.

3.2
"Frog"

As mentioned, the "frog" is the central component of a railway switch. The wheel load is transferred from a wing rail to the frog to allow a crossing maneuver. The cyclic response of the frog to continuous impacts is numerically investigated in [14]. This finite element model is used here to verify the HCT. Geometrical conditions for the contact are as follows: frog $R'_1 = 13.0$ mm, $R''_1 = \infty$; wheel $R'_2 = -160.0$ mm, $R''_2 = 558.0$ mm; $\varphi = 0°$.

The material of the frog and the wheel is first assumed to be elastic with $E = 210$ GPa and $\nu = 0.3$. An external normal compressive force F is chosen as 7.96×10^4 N. We consider here the static loading case. However, depending on the average velocity of the wheel, the jump in the inclination of the wheel-center path and the impacting mass, a momentum is suddenly transferred to the frog leading to a dynamic factor of three or more, for details see [15], [14]. Applying the HCT, we obtain $p_0 = 3.9$ GPa, $a = 10.0$ mm, $b = 1.0$ mm, $\alpha = 90°$.

The major axis of the contact ellipse extends along the longitudinal direction of the frog. This contact ellipse is long and narrow. The length of the major axis $2a$ is even larger than the curvature radius R'_1.

Both pure elastic contact and elastic-plastic contact are simulated numerically. The frog is mounted on a continuous bedding in our FE. The material of the wheel remains elastic while the frog consists of a high-strength material with $E = 178$ GPa and yield stresses $\sigma_{0.02} = 1.42$ GPa and $\sigma_{0.5} = 1.56$ GPa, described by a nonlinear kinematic hardening model, [16]. The shapes of the contact area from both the elastic and the elastic-plastic calculation look like narrow ellipses extending along the longitudinal direction of the frog. A quantitative comparison is carried out along the major and the minor axes of the theoretical ellipse as shown in Fig. 4. Again, the graph showing the contact pressure from the numerical calculation for the elastic contact agrees well with that from the HCT. Figure 4 indicates that plastic deformation reduces the contact pressure in the central part of the contact zone. The relation $p_0 \propto F^{1/3}$ is also checked for the numerical results and depicted in Fig. 5.

The HCT is applied in practice not only to determine the distribution of the contact pressure, but also to obtain the stress state in the contacting bodies. Both contact bodies are considered as elastic half-spaces in the HCT. The stress state in the bodies near the contact zone is, therefore, calculated from the contact pressure. Although the distribution of the contact pressure in the numerical contact calculation and in the HCT is nearly identical in the present case, it is reasonable to doubt the good agreement of the stress states in the frog with that in a half-space subjected to Hertz contact pressure, since the frog near the initial contact zone

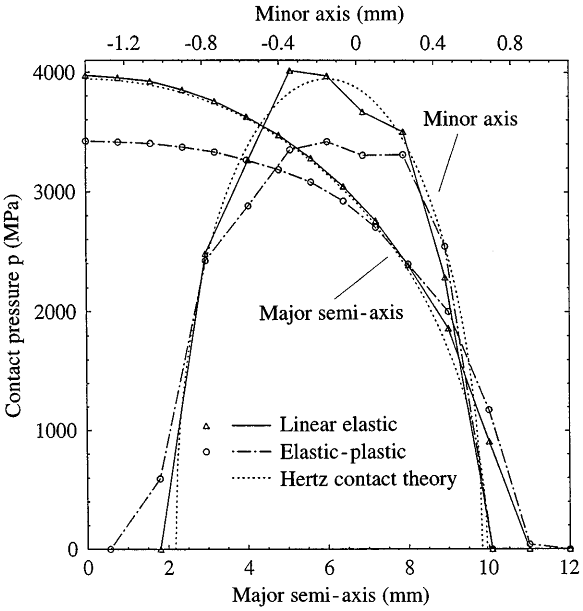

Fig. 4. Contact pressure distribution along the major semi-axis and the minor axis of the Hertz contact ellipse for the frog (major axis – frog's longitudinal direction; minor axis – frog's transverse direction)

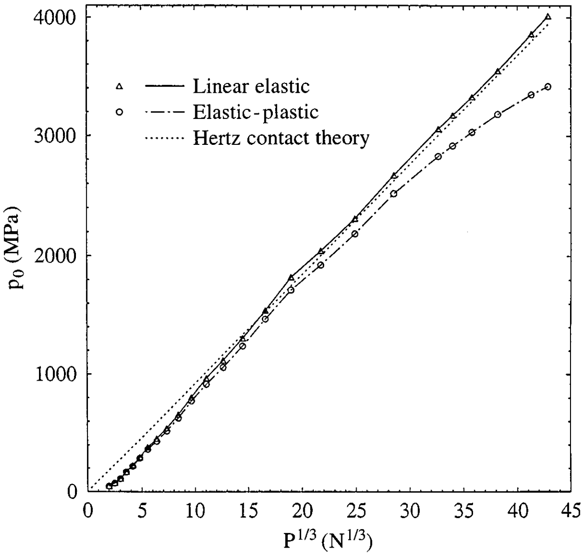

Fig. 5. Relation between the maximum contact pressure p_0 and the "1/3-power law" due to the external normal compressive force F for the frog

cannot be assumed to be a half-space. For comparison, the distributions of the von Mises equivalent stress σ_{eq} in the frog from the above numerical calculation and according to HCT are drawn in Fig. 6. Surprisingly, not only the maximum values and their corresponding positions but also the distributions coincide very well. The small discrepancy just beneath the contact surface is mainly due to the mesh density in the current configuration. Thus, the stress state in the subsurface region is also consistent with that from the HCT. For the sake of completeness, the von Mises equivalent stress from the above elastic-plastic calculation is also shown in Fig. 6. It is significantly smaller only in a limited region reaching from the surface to about 2.5 mm beneath the surface.

3.3
Rail UIC60

The UIC60 is the most common rail in Europe. Its transverse head profile consists of a sequence of circular arcs with three different radii of 300 mm, 80 mm and 13 mm. The sections of the profile on the 300 mm, 80 mm and 13 mm radii are referred to as the rail crown, rail shoulder and gauge corner, respectively. Due to the transverse movement of the wheel, initial contact may occur on each part of the profile. Here, four 3D FE contact models for different transverse contact positions are established for the rail UIC60 and the wheel UICORE. The rail

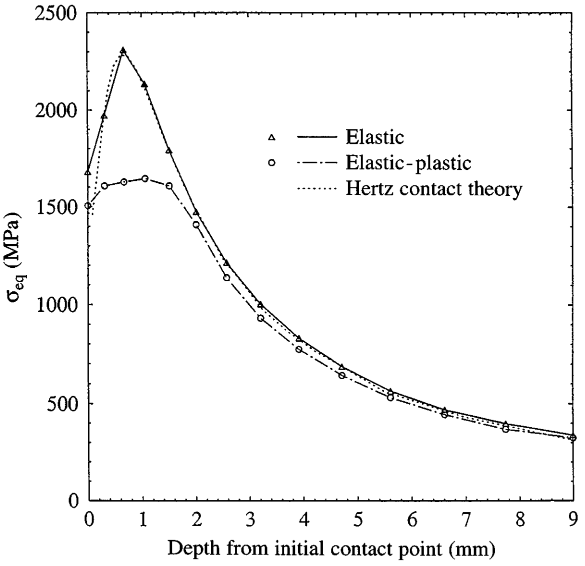

Fig. 6. Comparison of von Mises equivalent stresses σ_{eq} in the subsurface region for the frog

is mounted on discrete concrete sleepers, and the sleepers are placed on a ballast bedding in our calculation models. The initial longitudinal contact position lies in the middle between two sleepers in all the four models. Thus, there exists a symmetry of the problem for the four cases with respect to the longitudinal direction. The initial contact point is situated at the symmetry plane in each model. As an example, the whole FE mesh for model one is illustrated in Fig. 7. In order to obtain satisfying contact results, the meshes in the rail and the wheel near the contact zone have to be very fine in each of the four models.

The initial transverse contact positions for the four considered models are illustrated in Fig. 8. In the first position, Fig. 8a, the distance between the plane of the measure circle of the wheel and the middle plane of the rail is 15 mm. The initial contact point has a transverse distance of 6.6 mm to the middle plane of the rail and is located at the rail crown with 300 mm radius. In the second position, Fig. 8b, the distance between the plane of the measure circle of the wheel and the middle plane of the rail is 5 mm. The initial contact point lies at a transverse distance of 13.4 mm from the middle plane of the rail and is located at the rail shoulder having a radius of 80 mm. In the third position, Fig. 8c, the plane of the measure circle of the wheel and the middle plane of the rail coincide. The initial contact position has a transverse distance of 18.4 mm to the middle plane and is located at the profile of the rail shoulder with radius 80 mm. In the fourth position, Fig. 8d, the plane of the measure circle of the wheel is 2.5 mm to the left of the middle plane of the rail. The initial contact position is located at a transverse distance of

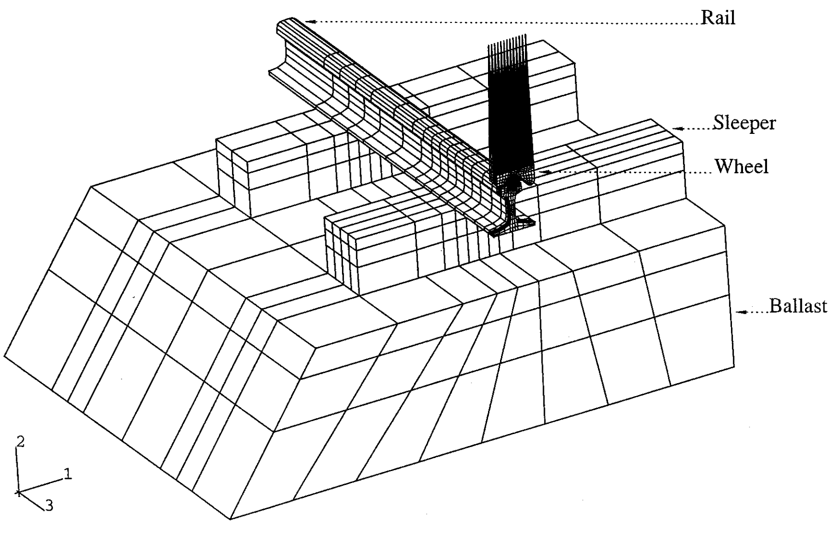

Fig. 7. Finite element mesh and profile of the whole analyzing model for position one of the rail UIC60

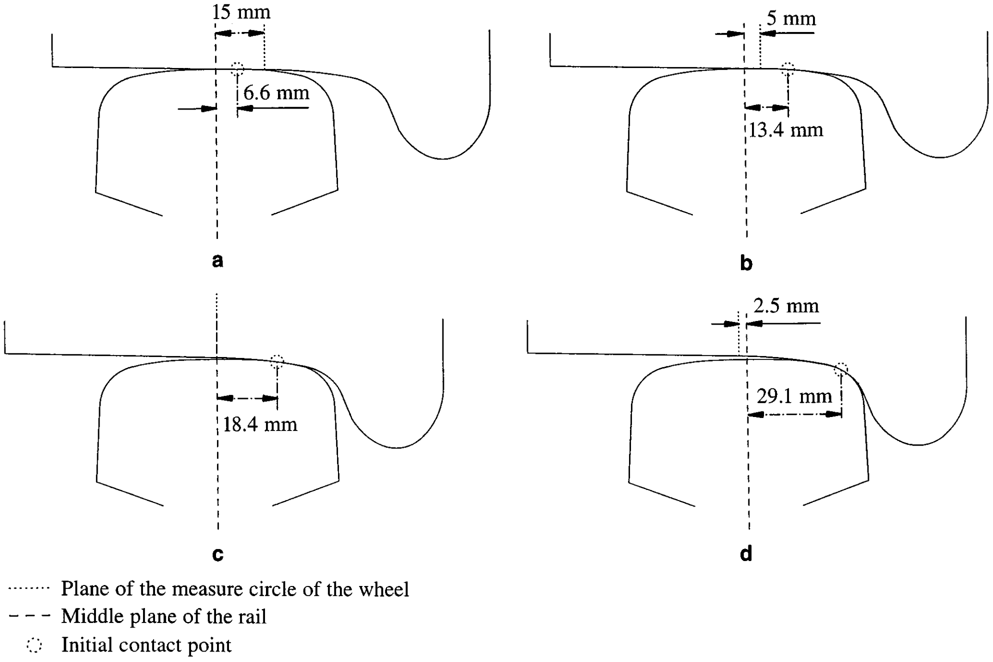

Fig. 8a–d. Contact position for rail UIC60 and wheel UICORE. **a** Position one; **b** position two; **c** position three; **d** position four

29.1 mm to the middle plane of the rail, at the gauge corner of the rail with radius 13 mm. The materials of the wheel and the rail are assumed as linear elastic with Young's modulus equal to 210 GPa and a Poisson ratio of 0.3. In the numerical calculations of elastic-plastic contact, only the rail is assumed as elastic-plastic with yield stresses $\sigma_{0.0} = 350.0$ MPa and $\sigma_{0.4} = 700.0$ MPa. An Armstrong–Frederick nonlinear kinematic hardening model is applied, [16]. The normal compressive force is 1.1025×10^5 N.

The distributions of the contact pressure determined by numerical calculations and the HCT for the first position, Fig. 8a, are shown in Fig. 9. The theoretical distribution agrees well with that from the numerical calculation of an elastic contact along the major axis of the theoretical contact ellipse. Figure 9 indicates that the calculated pressure distribution for the elastic contact is not symmetrical about the initial contact point. The minor semi-axis is a little shorter at the positive *y*-side, and the gradient of the pressure is much larger at the end of this

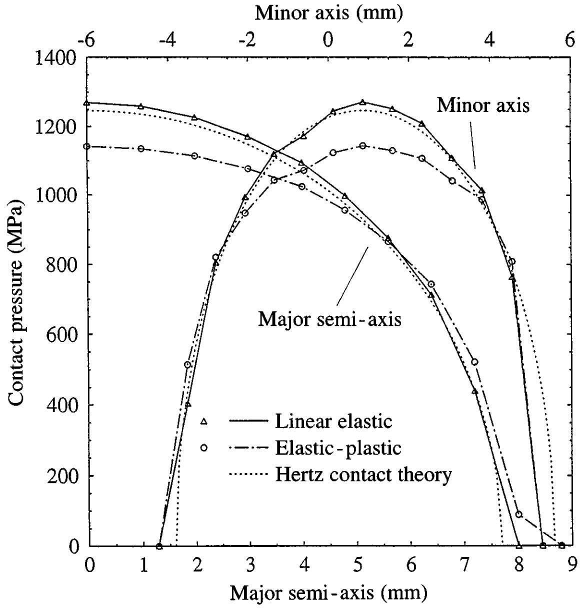

Fig. 9. Contact pressure distribution along the major axis and the minor semi-axis of the Hertz contact ellipse for position one Fig. 8a of the rail UIC60 (major axis – rail's longitudinal direction; minor axis – rail's transverse direction)

side. This is due to the fact that the contact area slightly exceeds the boundary of the rail crown with radius 300 mm and the rail shoulder with radius 80 mm. Such a deviation from the theoretical result due to the radius change in practical contact configuration becomes more pronounced in the next contact position.

The distributions of the contact pressure from numerical calculations and the HCT for position two, Fig. 8b, are shown in Fig. 10. The theoretical distribution again agrees well with the results from the numerical calculation of the elastic contact along the major axis. From Fig. 10, however, we can see that the size of the contact area in the transverse direction is much larger in numerical calculations than in the Hertz analysis, although the contact pressure near the contact center is identical both in the numerical calculation of elastic contact and in the analytical theory. Due to the extension of the contact area from the rail shoulder with radius 80 mm to the rail crown with radius 300 mm, the final contact area does not show any elliptical shape in numerical calculations. It looks like an ellipse with an additional part attached to it in the negative y-direction. The additional contact area becomes larger with increasing external load and it can disappear, if the external load is small enough. Similar results can be found in [17]. The subsurface stresses near the contact center from the numerical calculation of elastic contact should not be significantly different from those based on the HCT unless the external load is extremely large.

In position three, Fig. 8c, the contact area covers only the rail shoulder. The contact pressure from the numerical calculation for the elastic contact and from the HCT is nearly identical. Figure 11 shows its distribution along the minor axis of the theoretical contact ellipse. The contact pressure in the case of elastic-plastic contact in the center of the contact zone is smaller. The deviation at the edge of the contact zone emanates from the coarse mesh that has been used there.

Contact occurs at the gauge corner of the rail head in position four, Fig. 8d, with a minimum curvature radius 13 mm (which is the same as that in the case of the frog). The distributions of the contact pressure are shown in Fig. 12. The maximum contact pressure from both the numerical calculations and the HCT is remarkably higher than in the former contact position. The distribution of the contact pressure from numerical calculation in the case of elastic contact is still very similar to that from the HCT. However, the elastic-plastic pressure distribution is much smaller in the contact center due to large plastic deformation.

4
Dissipation power due to friction

The velocity components $\dot{s}_x, \dot{s}_y$ of the microslip between contacting points for steady rolling state have been derived in [9] as

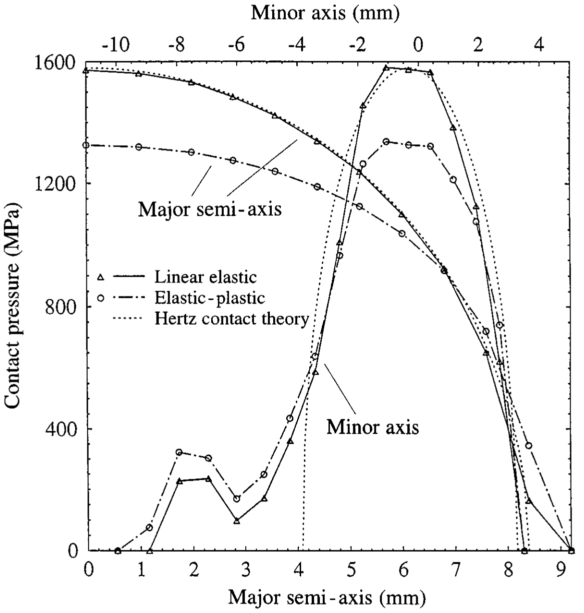

Fig. 10. Contact pressure distribution along the major semi-axis and the minor axis of the Hertz contact ellipse for position two Fig. 8b of the rail UIC60 (major axis – rail's longitudinal direction; minor axis – rail's transverse direction)

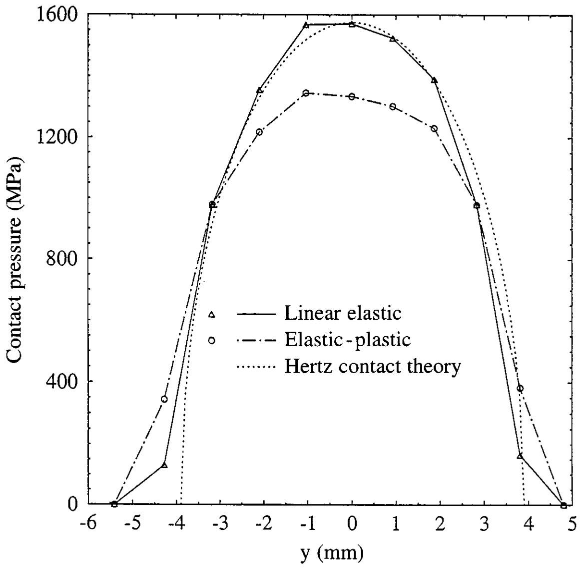

Fig. 11. Contact pressure distribution along the minor axis of the Hert contact ellipse for position three, Fig. 8c, of the rail UIC60 (minor axis – rail's transverse direction)

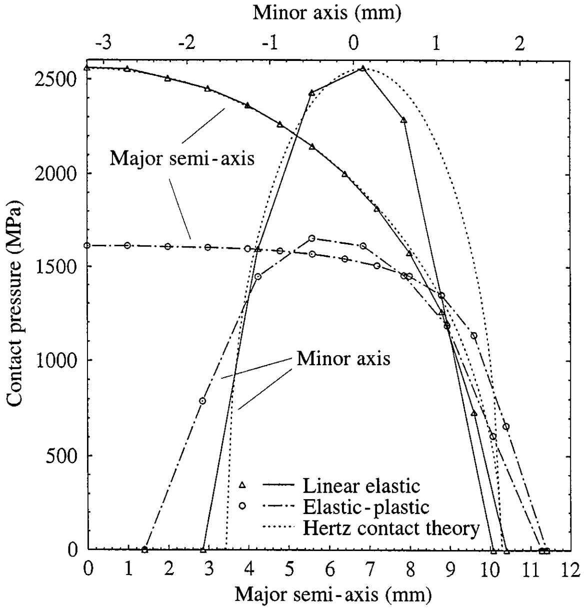

Fig. 12. Contact pressure distribution along the major axis and the minor semi-axis of the Hertz contact ellipse for position four, Fig. 8d of the rail UIC60 (major axis – rail's longitudinal direction; minor axis – rail's transverse direction)

$$\begin{aligned}\dot{s}_x(x,y) &= V\xi_x - \omega y + V\left(\frac{\partial u_x^{\mathrm{II}}}{\partial x} - \frac{\partial u_x^{\mathrm{I}}}{\partial x}\right),\\ \dot{s}_y(x,y) &= V\xi_y + \omega x + V\left(\frac{\partial u_y^{\mathrm{II}}}{\partial x} - \frac{\partial u_y^{\mathrm{I}}}{\partial x}\right) .\end{aligned}\tag{6}$$

Vector $\boldsymbol{\xi} = (\xi_x - \omega y/V, \xi_y + \omega x/V)$ is called the rigid slip, ξ_x, ξ_y are called creepages stemming from the difference in effective roll radii of the wheels, left and right, due to conicity, but also from the deformation of the wheel, for details see also [7]. The spinning velocity ω of a wheel with average radius R running on a straight rail with constant velocity V is V/R, while u_x^{II} and u_y^{II} are the components of the tangential elastic displacement at the contact surface of body II, u_x^{I} and u_y^{I} are the corresponding entities for body I. Here, the steady rolling state means that the phenomena are independent of explicit time in a properly chosen reference frame. The x-direction is chosen to be opposite to the rolling direction, the z-direction is the direction of the spinning vector of body II.

If the contact shear stresses applied at the contact surface of body II due to friction are denoted by $q_x(x,y)$ and $q_y(x,y)$, (the nomenclature contact shear stress has been taken from ABAQUS [11]) the density of the dissipation power d is defined as

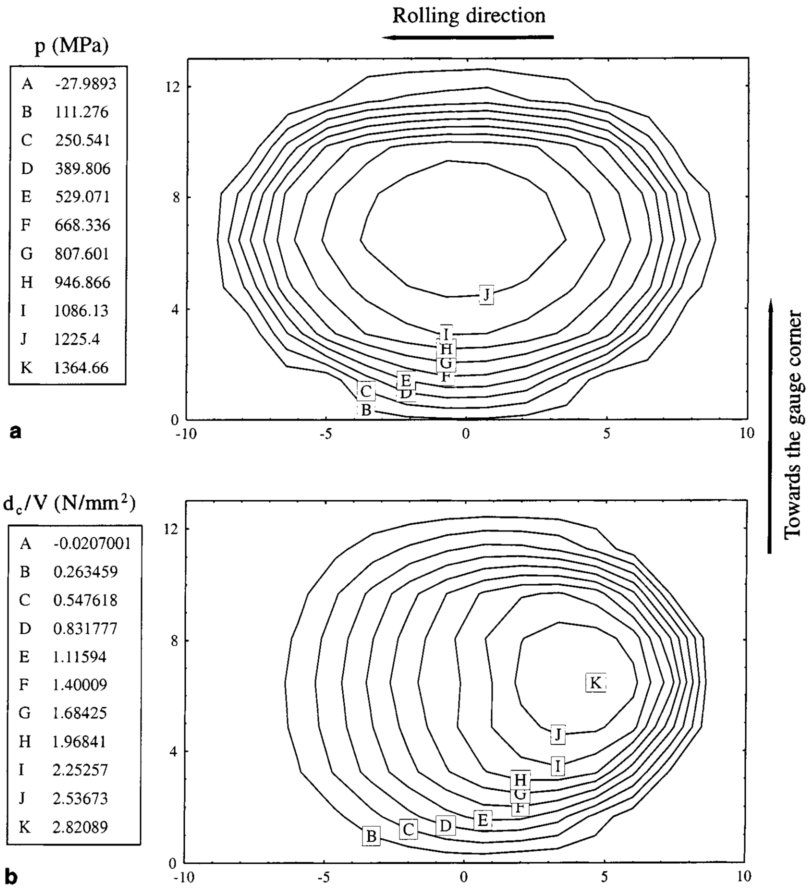

Fig. 13a, b. Comparison of the distribution of the contact pressure p and the density of the convective part of the dissipation power d_c/V for position one, Fig. 8a, with $\mu = 0.3$ **a** contact pressure; **b** density of the dissipation power

$$d = -(\dot{s}_x q_x + \dot{s}_y q_y) \ . \tag{7}$$

As the friction force is opposite to slip velocity, a minus has been added in Eq. (7). Thus, the total dissipation power D can be calculated by

$$D = \iint_C (d)\mathrm{d}C = -\iint_C (\dot{s}_x q_x + \dot{s}_y q_y)\mathrm{d}C \ . \tag{8}$$

Here, C represents the contact area.

Practically, contact occurs on a curved surface C in a 3D wheel-rail rolling contact configuration. A numerical calculation such as the FEM yields q_x and q_y as the contact shear stresses in the tangent plane at the local contact point, while $\dot{s}_x$ and $\dot{s}_y$ are the slip velocity components in the local tangent plane at the local contact point. Therefore, the above integral should be calculated with respect to the local coordinate system, changing with each contact point or contact element. For a recent discussion see [18]. In the following numerical calculations, the local coordinate system is chosen so that the x-coordinate is always opposite to the rolling direction. The initial contact points are assumed to be both the rolling and the spinning center. The goal of this chapter is to calculate the convective part of the dissipation power, which yields with (6)

$$d_c = -V\left[\left(\frac{\partial u_x^{\mathrm{II}}}{\partial x} - \frac{\partial u_x^{\mathrm{I}}}{\partial x}\right)q_x + \left(\frac{\partial u_y^{\mathrm{II}}}{\partial x} - \frac{\partial u_y^{\mathrm{I}}}{\partial x}\right)q_y\right] \ . \tag{9}$$

The derivatives of u_x, u_y can be taken directly from the computational results and would be identical if the classical HCT was applied substituting the contacting bodies by halfspaces.

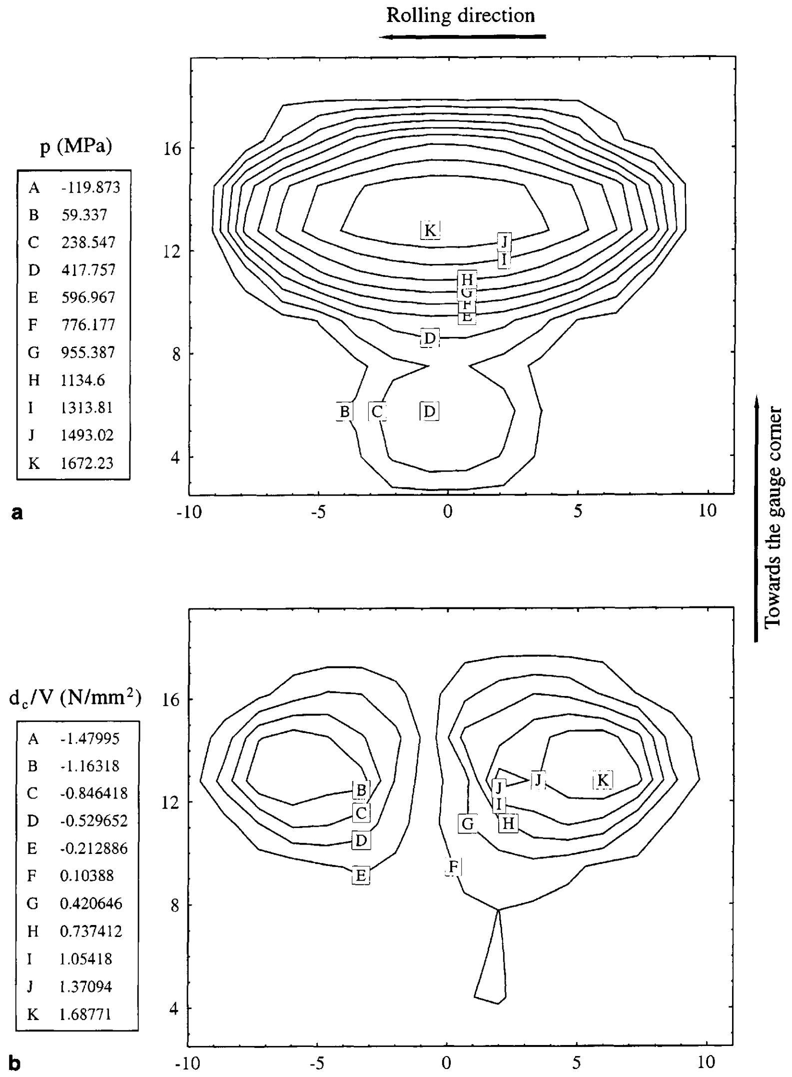

Fig. 14a, b. Comparison of the distribution of the contact pressure p and the density of the convective part of the dissipation d_c/V for position two, Fig. 8b, with $\mu = 0.3$ **a** contact pressure; **b** density of the convective part of the dissipation

The convective part of the total dissipation power follows as

$$D_c = \iint_C (d_c)\mathrm{d}C \ . \qquad (10)$$

The wheel (body II) is now assumed to be a locomotive wheel with a driving moment M applied on the wheel axis. We assume that the resultant horizontal force Q is μF which precludes a stick region. The driving moment M is then automatically calculated by the algorithm; μ is varied from 0.1 to 1.0.

Again the four contact configurations for the UIC60 rail and the UICORE wheel as in Sec. 3.3 are investigated, with a slightly increased force $F = 1.372 \times 10^5$ N against ($F = 1.1025 \times 10^5$ N in Sec. 3.3). The distribution of the contact pressure p together with that of the convective part of the dissipation power d_c are depicted in Fig. 13 for a "Hertz" configuration, corresponding to the position one of Fig. 8a, and a for a "non-Hertz" configuration, position two of Fig. 8b, in Fig. 14.

The distribution of the normalized density of the convective part of the dissipation power d_c/V is neither affine to the contact pressure nor is it comparable for all contact positions. The largest d_c/V always appears behind the contact center. It should be mentioned that some researchers, [19–21], assume that the heat-flow rate is proportional to the contact pressure. This assumption actually neglects the influence of the elastic deformation on the generation of

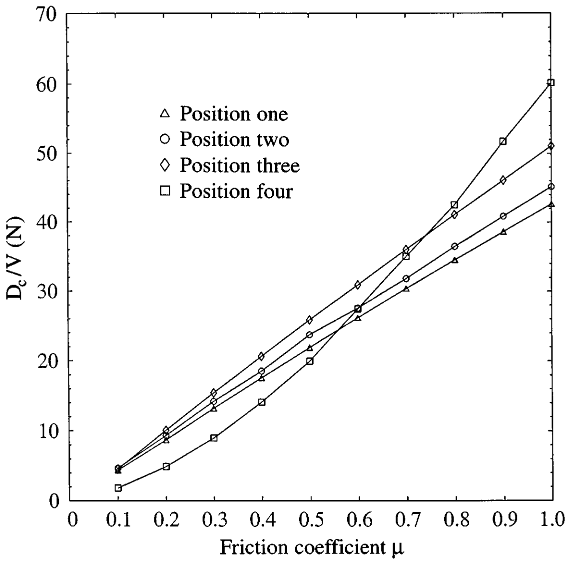

Fig. 15. Variation of the convective part of the normalized dissipation power D_c/V with friction coefficient μ

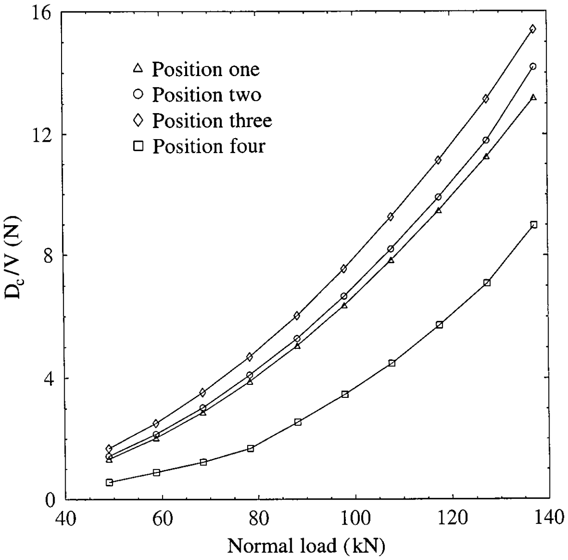

Fig. 16. Variation of convective part of the normalized dissipation power with applied normal load for given friction coefficient $\mu = 0.3$

the energy dissipation. The convective part of the total dissipation power depending on the friction coefficient μ is depicted in Fig. 15, and on the load for $\mu = 0.3$ in Fig. 16. Obviously, the configuration according to position four of Fig. 8d shows a different tendency as opposed to the configurations one to three, Figs. 8a–c. This stems from the fact that the surface curvature changes during the contact from the shoulder curvature (radius 80 mm) to the crown curvature (radius 300 mm).

One may establish a simple relation for D_c as

$$D_c \propto cV\mu\left(\frac{F}{F_{ref}}\right)^{\alpha} , \qquad (11)$$

with α being ca. 2.0 and c being a constant with the dimension N; F_{ref} can be set to 40 kN. However, one must keep in mind that the configuration due to position four, Fig. 8d deviates from this proposal.

5
Conclusion

Three-dimensional FE calculations for rail-wheel contact problems for different types of rails and wheels and for different contact positions have been carried out. Not only the elastic contact but also the elastic-plastic contact has been considered. The numerical results have been compared with those of the HCT for purely elastic contact.

In the case of an elastic wheel and rail, the distribution of the contact pressure from the numerical calculations of the elastic contact agrees well with that from the HCT, if the surface curvature of the rail does not change inside the contact area. This, however, is possible for some realistic positions of the wheel on the rail. It is interesting to note that the HCT applies well even in those cases, where one of the minimum curvature radii of the contacting bodies is smaller than the dimension of the contact area. The subsurface stress states from the numerical calculation for the elastic contact and from the HCT also agree well. That means, that the HCT can be applied in rail-wheel contact problems with reasonable accuracy if the material is assumed as linear elastic and the surface curvature of the rail remains unchanged.

A significant deviation, however, occurs if plastic deformation appears in the rails. The contact pressure distribution is higher than the semi-ellipsoidal, but much flatter. The highest contact pressure is always less than that from the Hertz theory of elastic contact. This discrepancy becomes more obvious with increasing plastic deformation, i.e. external loading.

Finally, the dissipation power due to the difference in the local deformation velocities has been investigated. The HCT cannot produce any such data since it assumes two halfspaces as contacting bodies which do not represent any real configuration of a rail and a wheel or a switch component.

References

1. **Hertz, H.:** Über die Berührung fester elastischer Körper. J. reine und angewandte Mathematik 92 (1882) 156–171
2. **Farris, T. N.; Keer, L. M.; Steele, R. K.:** The effect of service loading on shell growth in rails. J. Mech. Phys. Solids 35 (1987) 667–700
3. **Farris, T. N.; Keer, L. M.; Steele, R. K.:** Life prediction for unstable shell growth in rails. Trans. ASME, J. Eng. Indust. 112 (1990) 175–179
4. **Ekberg, A.; Bjarnehed, H.; Lundén, R.:** A fatigue life model for general rolling contact with application to wheel/rail damage. Fatigue Fracture Eng. Mat. Struct. 18 (1995) 1189–1199
5. **Moyar, G. J.; Steele, R. K.:** A practical method for predicting the effect of material properties and residual stresses on rail subsurface fatigue initiation. In: Brammfitt, B. L. (ed.) Proc. Int. Symp. Rail Steels for the 21st Century, pp. 121–129. Warrendale: Iron and Steel Society 1995
6. **Kalker, J. J.:** Three-dimensional elastic bodies in rolling contact, Dordrecht: Kluwer Academic Publications 1990
7. **Kalker, J. J.:** Wheel-rail rolling contact theory. Wear 144 (1991) 243–261
8. **Yu, C. -C.; Keer, L. M.; Steele, R. K.:** Three-dimensional residual stress effects on the fatigue crack initiation in rails. Trans. ASME, J. Trib. 119 (1997) 660–666
9. **Bogdanski, S.; Olszak, M.; Stupnicki, J.:** Numerical stress analysis of rail rolling contact fatigue cracks. Wear 191 (1996) 14–24
10. **Johnson, K. L.:** Contact Mechanics. Cambridge: Cambridge University Press 1985
11. **Hibbitt, Karlsson, Sorensen, Inc.:** ABAQUS User Manual, Version 5.6, Pawtucket, 1996
12. **Cooper, D. H.:** Hertzian contact-stress deformation coefficients. Trans. ASME, J. Appl. Mech. 36 (1969) 296–302
13. **Mroz, Z.:** An attempt to describe the behavior of metals under cyclic loads using a more general workhardening model. Acta Mech. 7 (1969) 199–212
14. **Yan, W.; Antretter, T.; Fischer, F. D.; Blumauer, H.:** Numerical analysis of the cyclic response of a crossing component in a switch, Report 286, Christian Doppler Laboratorium für Funktionsorientiertes Werstoff-Design, 1999
15. **Fischer, F. D.; Steiner, H.; Schossmann, R.:** Zur Ermittlung der Spannungen im Radüberlaufsbereich von Herzstückspitzen. Eisenbahntechnische Rundschau (ETR) 28 (1979) 597–602
16. **Armstrong, P. J.; Frederick, C. O.:** A mathematical representation of the multiaxial Bauschinger effect, Report RD/B/N. 731, Central Electricity Generating Board 1966
17. **Le The, H.:** Normal- und Tangentialspannungsberechnung beim rollenden Kontakt für Rotationsköper mit nichtelliptischen Kontaktflächen. Fortschritt-Berichte VDI., Reihe 12: Verkehrstechnik/Fahrzeugtechnik. Düsseldorf: VDI Verlag GmbH 1987
18. **Piotrowski, J.; Kik, W.:** On calculation of creep forces generated within weakly curved area of contact of wheel and rail. In: VDE/Tagungsband Bahn-Bau '98, Berlin (1998) 98–109
19. **Knothe, K.; Liebelt, S.:** Determination of temperature for sliding contact with applications for wheel-rail systems. Wear 189 (1995) 91–99
20. **Fischer, F. D.; Werner, E.; Yan, W.:** Thermal stresses for frictional contact in wheel-rail systems. Wear 211 (1997), 156–163
21. **Gupta, V.; Hahn, G. T.; Bastias, P. C.; Rubin, C. A.:** Calculations of the frictional heating of locomotive wheel attending rolling plus sliding. Wear 191 (1996) 237–241